Tunable Crossed Andreev Reflection and Elastic Cotunneling in Hybrid Nanowires

Bordin, Alberto; Wang, Guanzhong; Liu, Chun Xiao; Ten Haaf, Sebastiaan L.D.; Van Loo, Nick; Mazur, Grzegorz P.; Xu, Di; Van Driel, David; Zatelli, Francesco; Gazibegovic, Sasa

DOI
10.1103/PhysRevX.13.031031

Publication date
2023

Document Version
Final published version

Published in
Physical Review X

Citation (APA)
Bordin, A., Wang, G., Liu, C. X., Ten Haaf, S. L. D., Van Loo, N., Mazur, G. P., Xu, D., Van Driel, D., Zatelli, F., Gazibegovic, S., Badawy, G., Bakkers, E. P. A. M., Wimmer, M., Kouwenhoven, L. P., & Dvir, T. (2023). Tunable Crossed Andreev Reflection and Elastic Cotunneling in Hybrid Nanowires. *Physical Review X*, *13*(3), Article 031031. https://doi.org/10.1103/PhysRevX.13.031031

Featured in Physics

Tunable Crossed Andreev Reflection and Elastic Cotunneling in Hybrid Nanowires

Alberto Bordin,[1] Guanzhong Wang,[1] Chun-Xiao Liu,[1] Sebastiaan L. D. ten Haaf,[1] Nick van Loo,[1] Grzegorz P. Mazur,[1] Di Xu,[1] David van Driel,[1] Francesco Zatelli,[1] Sasa Gazibegovic,[2] Ghada Badawy,[2] Erik P. A. M. Bakkers,[2] Michael Wimmer,[1] Leo P. Kouwenhoven,[1] and Tom Dvir[1,*]

[1]*QuTech and Kavli Institute of NanoScience, Delft University of Technology, 2600 GA Delft, Netherlands*
[2]*Department of Applied Physics, Eindhoven University of Technology, 5600 MB Eindhoven, Netherlands*

(Received 18 January 2023; accepted 26 July 2023; published 15 September 2023)

A short superconducting segment can couple attached quantum dots via elastic cotunneling (ECT) and crossed Andreev reflection (CAR). Such coupled quantum dots can host Majorana bound states provided that the ratio between CAR and ECT can be controlled. Metallic superconductors have so far been shown to mediate such tunneling phenomena, albeit with limited tunability. Here, we show that Andreev bound states formed in semiconductor-superconductor heterostructures can mediate CAR and ECT over mesoscopic length scales. Andreev bound states possess both an electron and a hole component, giving rise to an intricate interference phenomenon that allows us to tune the ratio between CAR and ECT deterministically. We further show that the combination of intrinsic spin-orbit coupling in InSb nanowires and an applied magnetic field provides another efficient knob to tune the ratio between ECT and CAR and optimize the amount of coupling between neighboring quantum dots.

DOI: 10.1103/PhysRevX.13.031031

Subject Areas: Condensed Matter Physics, Semiconductor Physics, Superconductivity

The Kitaev chain is a prime example of condensed-matter toy models exhibiting a topological superconducting phase [1]. Practical proposals to construct an artificial Kitaev chain require a set of quantum dots (QDs) separated by narrow superconducting segments [2–4]. Such QDs interact via two mechanisms: crossed Andreev reflection (CAR) and elastic cotunneling (ECT). In CAR, electrons from two separate QDs tunnel into the superconductor, forming a Cooper pair; or, in its reversed process, a Cooper pair is split into two electrons, tunneling to different QDs [see the schematic in Fig. 1(a)] [5–7]. ECT occurs when a single electron tunnels between the two QDs via the superconductor [see the schematic in Fig. 1(b)]. The balance between CAR- and ECT-induced couplings is crucial for observing poor man's Majorana zero modes at the boundaries of a two-site Kitaev chain [3], recently observed in Ref. [8]. Furthermore, precise control over the interplay between CAR and ECT is crucial for achieving high-fidelity entanglement generation through Cooper-pair splitting [5,9]. Moreover, this control can serve as an efficient mechanism for coupling spin qubits over longer length scales beyond those achievable through exchange coupling [10–14].

Semiconductor-superconductor hybrids are the primary platform to study CAR and ECT [16–19] due to their unique ability to form QDs in semiconductors and effectively couple them to superconductors. These hybrids enable the formation of Andreev bound states (ABSs), where a confined semiconducting level is tunnel coupled to a superconductor. An important characteristic of ABSs is their ability to transition smoothly from electronlike to holelike excitations through electrostatic gating [20–22]. ABSs can further replace metallic superconductors in facilitating CAR and ECT processes between adjacent QDs [23]. It is predicted that the interplay between the electron and hole components of an ABS plays a crucial role in controlling CAR and ECT phenomena [24]. Furthermore, the presence of an external magnetic field impacts the energy of ABSs through Zeeman splitting [25], thereby influencing the amplitudes of CAR and ECT. Notably, in the presence of spin-orbit coupling, the dependence of these amplitudes on the magnetic field direction becomes anisotropic [15,26].

Scaling the Kitaev chain from the two-QD system discussed in Ref. [8] to many QDs requires a deterministic control of the CAR and ECT coupling between neighboring QDs. The interplay of CAR and ECT and the ABS mediating them provides the means to achieve such control. To this date, this interplay was never demonstrated.

*tom.dvir@gmail.com

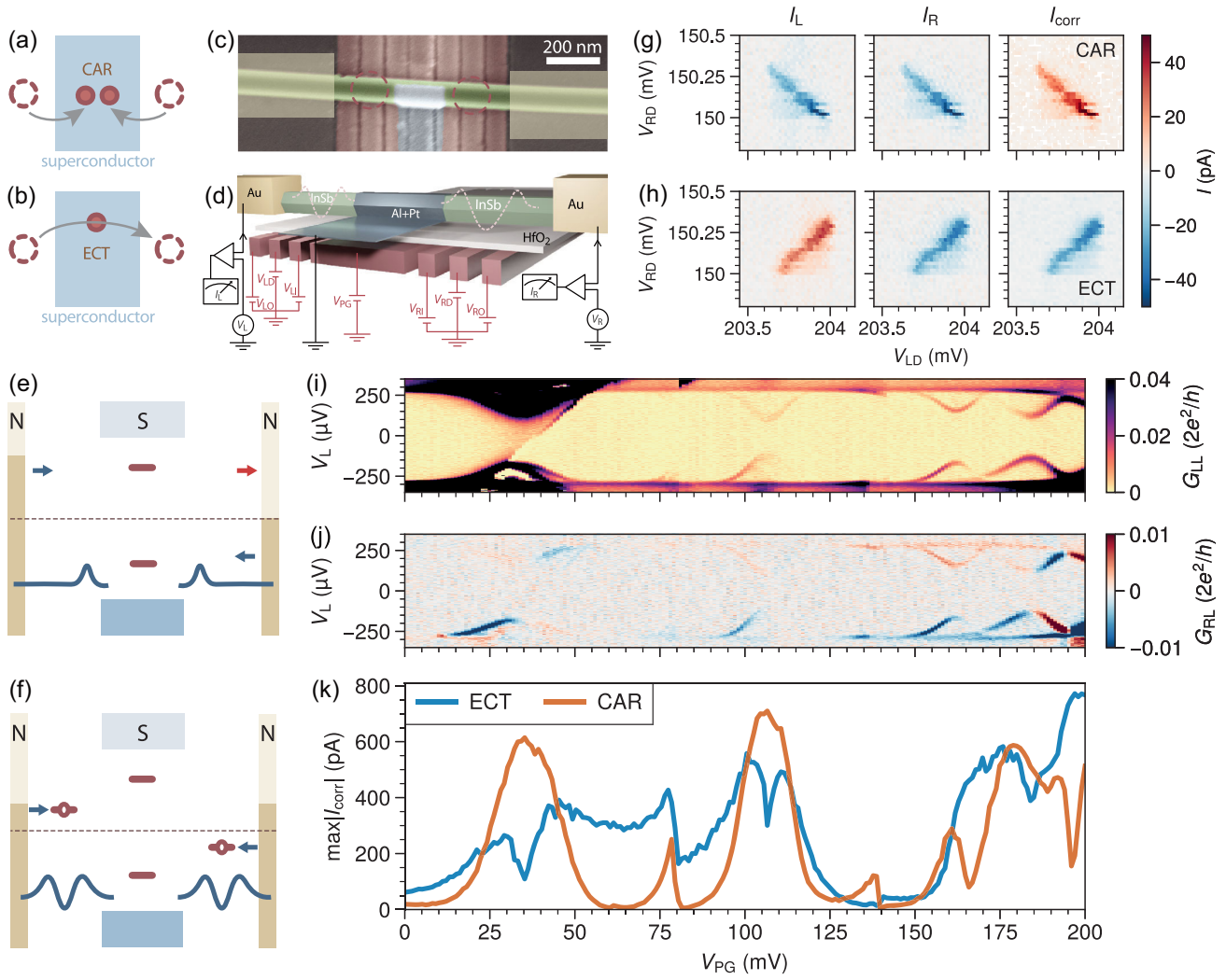

FIG. 1. Correlation between ABS and CAR or ECT processes. (a),(b) Illustration of the ECT (a) and CAR (b) processes. (c) Scanning electron micrograph of device *A*. (d) Schematic illustration of our devices and experimental setup. An InSb nanowire (green) is coated by a thin Al shell (blue, Al + Pt for device *A*), on top of seven finger gates (red). Two Cr/Au leads (yellow) are attached to both sides of the wire. (e) Spectroscopy configuration: Yellow bars depict voltage bias in normal (*N*) contacts, while blue rectangles represent the superconductor (*S*). Blue curves sketch the desired voltage profile defined with the gates; voltage barriers are not to scale. (f) Configuration with QDs: Applying low voltages on V_{LO},V_{LI} and V_{RI},V_{RO} forms a QD on the left and right side of the superconducting segment. (g),(h) Measurement of the ECT-induced current (g) and the CAR-induced current (h), as in Ref. [15], around a charge degeneracy point. (i) G_{LL} as a function of V_L and V_{PG} when setting the gates in the tunneling spectroscopy configuration. (j) G_{RL} as a function of V_L and V_{PG} in the same settings as (b). G_{LL} and G_{RL} are calculated by taking the numerical derivative after applying a Savitzky-Golay filter of window length 11 and polynomial order 1 to the measured I_L and I_R currents, respectively. (k) CAR- and ECT-induced currents as a function of V_{PG} measured using the $N \leftrightarrow N+1$ transition in both QDs. The values of V_{LI} and V_{RI} are kept constant during measurements in (b), (c), and (e).

In this work, we report on gate tunability of CAR and ECT in hybrid semiconductor-superconductor heterostructures. In particular, both processes are correlated with the presence of ABSs in the hybrid. By comparing experimental data and our theoretical model, we further show that the observed CAR and ECT amplitudes, respectively, result from constructive and destructive interference of tunneling paths. The interference pattern is linked to the charge of the mediating Andreev bound state and can be controlled via tuning the hybrid's chemical potential. Finally, we report on the magnetic field dependence of CAR and ECT. We show how the CAR and ECT interference patterns are modified through the interplay of the orientation of the magnetic field, the direction of the spin-orbit coupling, the energy of the ABS, and its spin splitting.

Figure 1(c) shows a scanning electron microscope image of device *A*, while in Fig. 1(d) we show a schematic

illustration of the device and the measurement circuit. An InSb nanowire is deposited on prefabricated metallic gates (separated from the nanowire by a thin dielectric layer). Using the shadow lithography technique [27,28], a thin superconducting layer is deposited on top of the middle segment of the nanowire. Normal contacts are then fabricated on each side of the device. Details of the fabrication are described in Supplemental Material [29]. The chemical potential of the semiconducting-superconducting hybrid is controlled by the plunger gate underneath (V_{PG}). The bare nanowire segments on both sides of the hybrid are regulated by three finger gates each. To measure the spectrum of the hybrid segment using tunnel spectroscopy, we create a single tunnel barrier on each side, as depicted in Fig. 1(e). In contrast, to establish QDs on either side of the hybrid segment, we further reduce the voltage applied to the gates adjacent to the normal leads. This is done while maintaining the voltages applied to the gates neighboring the hybrid segment at fixed levels, as illustrated in Fig. 1(f). The chemical potential of the QDs is controlled by the middle finger gates on the left and right bare nanowire segments (V_{LD} and V_{RD}).

Transport measurements are carried out by applying dc voltage biases on the left and the right contacts (V_L and V_R, respectively) and measuring the resulting dc currents on both sides (I_L and I_R). Local ($G_{LL} = dI_L/dV_L$, $G_{RR} = dI_R/dV_R$) and nonlocal ($G_{RL} = dI_R/dV_L, G_{LR} = dI_L/dV_R$) conductances are obtained as numerical derivatives of the dc currents unless otherwise specified. All measurements are conducted in a dilution refrigerator with a measured electron temperature of approximately 50 mK. We characterize the QDs by measuring the gate-dependent and magnetic-field-dependent transport through them and focus in the remainder of this paper on two charge transitions of each QD: from N to $N+1$ electrons and $N+1$ to $N+2$ electron, where N is a small even integer (see Fig. S1 [29]).

The experiments described in Refs. [8,15] are primarily conducted using the device displayed in Fig. 1(c). In Ref. [15], the focus is on investigating spin precession in CAR and ECT for a fixed value of the plunger gate (V_{PG}). The values for the tunnel gates are consistent with the settings used in this research. In contrast, Ref. [8] utilizes barrier gates set to a more transparent configuration to boost effective coupling between the formed QDs. The phenomena reported here are measured using four devices, three of them discussed in this manuscript and in the Supplemental Material [29] (see Fig. S2 [29] for scanning electron imaging of the three devices).

We begin by describing our measurement method for CAR and ECT, the focus of this manuscript. Since the hybrid segment supports both processes, we turn to the applied bias to distinguish between them [17]. The CAR- and ECT-induced currents (I_{CAR} and I_{ECT}, respectively) are measured using a method introduced in our previous work [15]. In CAR, electrons exhibit a correlated flow, moving either inward toward the hybrid segment to form a Cooper pair or outward when a Cooper pair is broken. This correlation is facilitated by applying the same bias to both the right and left leads. To measure the CAR-induced currents at a specific value of V_{PG}, we apply a fixed bias of $V_L = V_R = 70\ \mu V$ to both leads and scan V_{LD} and V_{RD} within a range of approximately 1 mV around the charge degeneracy point of each dot. In Fig. 1(g), we present the measured I_L and I_R currents alongside the correlated current $I_{corr} \equiv \mathrm{sgn}(I_L I_R)\sqrt{|I_L I_R|}$. We observe a current feature that maximizes along a diagonal with a negative slope, indicating opposite chemical potentials of the two QDs. CAR-induced currents occur when V_{LD} and V_{RD} satisfy the condition that the chemical potentials of both QDs have equal magnitudes but opposite signs with respect to the Fermi energy [shown schematically in Fig. 1(f)], consistent with the observation.

In ECT, electrons enter the device through one lead and exit through the other, requiring an antisymmetric bias configuration. To measure the amount of ECT-induced currents, we thus repeat the procedure described above when applying antisymmetric bias on both leads: $V_L = -V_R = 70\ \mu V$. Figure 1(h) shows the ECT-induced current, displaying a current feature with a positive diagonal, consistent with both QDs being resonant with each other.

We emphasize that we observe current only when both QDs are within the bias window. The absence of a subgap current through a single QD indicates that the charging energy of the QDs is sufficient to suppress electron-hole correlation on the QDs.

In this manuscript, as in Ref. [15], the maximum of I_{corr} is taken as a proxy of the CAR strength $I_{CAR} \equiv \max(I_{corr})$, and minus the minimum of I_{corr} is taken as a proxy of the ECT strength $I_{ECT} \equiv -\min(I_{corr})$. For every CAR and ECT measurement, we make sure that the bias voltages V_L and V_R are smaller than the ABS energy.

We now turn our attention to the spectrum of the hybrid semiconducting-superconducting segment. To measure tunnel spectroscopy, we form a single tunnel barrier on each side of this segment, as shown schematically in Fig. 1(e). Figure 1(i) shows that, at low values of V_{PG}, the spectrum features a hard superconducting gap. Increasing V_{PG} leads to the formation of discrete ABSs under the superconducting film appearing as electron-hole symmetric subgap peaks. These peaks also appear in the nonlocal conductance [Fig. 1(j)], indicating that the ABSs extend throughout the hybrid segment [30].

Next, to measure currents induced by CAR and ECT (I_{CAR} and I_{ECT}), we form a QD on each side of the hybrid segment as explained above. Figure 1(k) shows the dependence of I_{CAR} and I_{ECT} on V_{PG} when both QDs are tuned to the $N \leftrightarrow N+1$ transition (see Fig. S3 [29] for data involving $N+1 \leftrightarrow N+2$ transitions and the discussion of the effect of Pauli spin blockade). Both currents respond strongly to changes in V_{PG}, suggesting that they originate from processes that involve the hybrid segment.

I_{CAR}, in particular, reaches peak currents at V_{PG} values where ABSs in the hybrid segment reach a minimal energy. In regions of V_{PG} far from ABSs, I_{CAR} and I_{ECT} are suppressed. These observations hold for all devices we measured (see Fig. S4 [29] for another example).

To understand the role of ABSs in mediating CAR- and ECT-induced currents, we consider a model with two QDs on each side of a single ABS confined in the central hybrid segment, as shown in Figs. 2(a) and 2(b). Considering only one orbital state in each QD, this reduces to a simple three-site model [24,31,32]. For simplicity, we treat the ABS as one pair of semiconducting states tunnel coupled to the superconductor in the atomic limit [33], simplifying the general expressions derived in Ref. [24] (see Supplemental Material [29] for details). Andreev reflection at the semiconductor-superconductor interface hybridizes the two electronic states with even charge occupation, $|0\rangle$ and $|2\rangle$, with hybridization rate Γ. The ground state of the ABS is a spin singlet of the form $|S\rangle = u|0\rangle - v|2\rangle$, where u, $v > 0$ are the normalized superposition coefficients determined by Γ and μ, the chemical potential of the electronic level before hybridization. Positive μ results in $u > v$, and negative μ leads to $u < v$ [33]. The excited states of the ABS form a doublet $|D\uparrow\rangle, |D\downarrow\rangle$, where $\uparrow$ and $\downarrow$ indicate, in the absence of spin-orbit coupling, the spin state of the single electron occupying the ABS (see Supplemental Material [29] for general spin-orbit-coupled scenarios).

Under zero external magnetic field, the doublet states are degenerate and the energy difference between $|S\rangle$ and $|D\rangle$ is E_{ABS}, which reaches a minimum around $\mu = 0$ [Fig. 2(c)] [33]. An excitation from the ground state of the ABS to an excited state is said to be a Bogoliubov quasiparticle, having an electronlike part u and a holelike part v in superposition. The effective charge of the ABS is defined as the net charge character of this excitation, $-e(u^2 - v^2)$, where $e > 0$ is the elementary charge [20–22]. This quantity ranges from $-e$ (electronlike) to $+e$ (holelike).

We consider both CAR and ECT as coherent second-order processes that involve the virtual occupation of an ABS doublet as the intermediate state. ECT can take place through two paths. The first, marked in gray in Fig. 2(a), involves the occupation of the ABS by adding an electron from one lead with a hopping amplitude proportional to u, followed by emptying of the ABS via ejection of the electron to the other lead, with an amplitude also proportional to u. The second, marked by the dashed green arrow in Fig. 2(a), occurs in the opposite order: An ABS is excited to $|D\rangle$ by accepting a hole from one lead, with an amplitude proportional to v, and then relaxes to $|S\rangle$ by ejecting a hole to the other lead, also with an amplitude proportional to v. As presented in Ref. [24] and briefly here in Supplemental Material [29], these two paths interfere destructively due to fermion exchange statistics, and the ECT-induced current I_{ECT} is

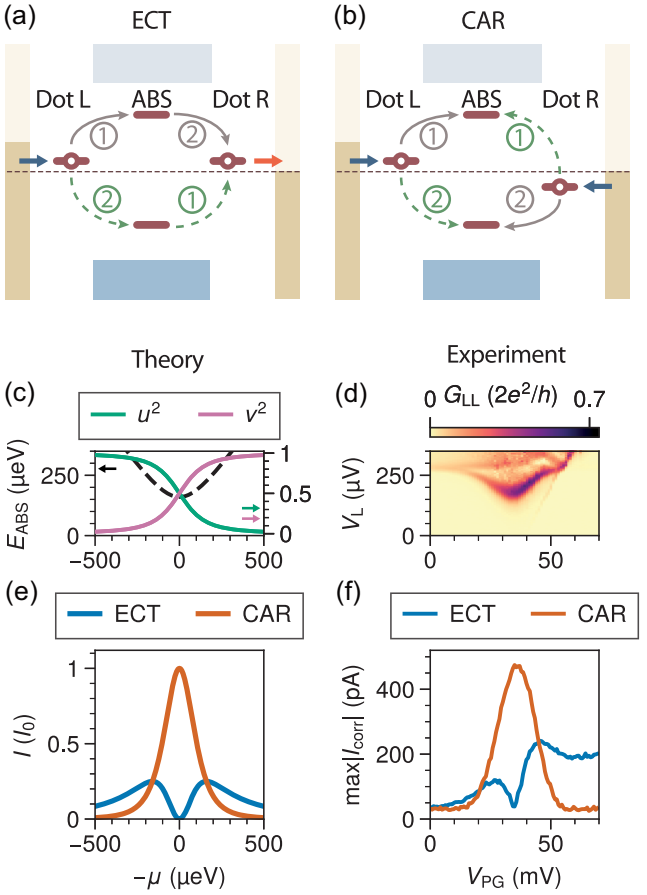

FIG. 2. Detailed study of CAR and ECT through an ABS. (a) Two possible paths for ECT: An electron hops from the left QD to the center ABS, followed by an escape from the ABS to the right QD (solid gray arrow), and the processes in the opposite order (dashed green arrow). (b) Two possible paths for CAR: An electron from the left QD enters the ABS followed by another electron arriving from the right QD (solid gray arrow) and the same processes in reversed order (dashed green arrow). (c) E_{ABS}, and u, v as a function of μ calculated in the atomic limit, where $E_{ABS} = \sqrt{\Gamma^2 + \mu^2}$ with $\Gamma = 160$ μeV [33]. μ and V_{PG} are related via $\mu = -e\alpha(V_{PG} - V_0)$, where α is the gate lever arm and $V_0 = 35$ mV is an offset. Comparing data to theory, we estimate $\alpha \sim 0.01$. (d) G_{LL} as a function of V_L and V_{PG} showing a single ABS. (e) A toy-model calculation of the transmission probability as a function of μ. (f) A high-resolution measurement of CAR and ECT amplitudes while tuning V_{PG}. The background noise level is approximately 30 pA (see Supplemental Material [29]).

$$I_{ECT} = I_0 \left| \frac{u^2 - v^2}{E_{ABS}/\Gamma} \right|^2, \tag{1}$$

where I_0 is a proportionality constant given by $I_0 = (e/\hbar) \cdot (t_L^2 t_R^2/\Gamma^2 \gamma_{DL})$ and depends on the coupling between the QDs and the ABS (t_L and t_R) as well as the lifetime of QDs due to coupling to the leads (γ_{DL}) in the limit of electron temperature and tunnel couplings much smaller than bias voltage. Strikingly, the destructive interference results

in a suppression of I_{ECT} near $\mu = 0$ where $u^2 = v^2 = \frac{1}{2}$ [Fig. 2(e)].

The process of CAR, depicted in Fig. 2(b), can take place via two paths as well. In the first path (marked by the dashed green arrow), an electron from the left lead populates the ABS with an amplitude proportional to u, followed by emptying of the ABS via accepting an electron from the right lead, with an amplitude proportional to v. In the second path, the roles of the left and right QDs are reversed. The two paths interfere constructively, yielding

$$I_{\mathrm{CAR}} = I_0 \left| \frac{2uv}{E_{\mathrm{ABS}}/\Gamma} \right|^2, \tag{2}$$

where I_{CAR} is the CAR-induced current, shown in Fig. 2(e). The term uv is significant only when $|\mu|$ is small, leading to the peak in I_{CAR} around $\mu = 0$ [Fig. 2(e)]. This is also where ECT is diminished, allowing CAR to dominate over ECT. Far away from ABS charge neutrality, ECT decays slower than CAR and becomes the dominant coupling mechanism, as it does not require electron-hole conversion to take place. The distinct dependencies of CAR and ECT on μ thus enable us to tune the relative strengths between them via electrostatic gating.

To study our model experimentally, we focus on the range of V_{PG} values between 0 and 70 mV where a single ABS dominates the subgap spectrum [Fig. 2(d)]. The ABS reaches a minimum around $V_{\mathrm{PG}} = 35$ mV and merges with the superconducting gap below $V_{\mathrm{PG}} = 10$ mV and above $V_{\mathrm{PG}} = 60$ mV. Figure 2(f) shows I_{CAR} and I_{ECT} measured in the same V_{PG} range with higher resolution in V_{PG} than Fig. 1(e). As predicted, I_{CAR} features a narrow peak centered around the ABS energy minimum. I_{ECT} is nonzero in a wider range of V_{PG} values and, as predicted, shows a dip when the ABS energy is minimal. We interpret this suppression as resulting from the destructive interference of the two ECT paths. We emphasize that this quantum mechanical interference is distinct from the cancellation between electron and hole currents as observed in three-terminal spectroscopy of hybrid nanowires [22,34]. Note that, contrary to our theoretical model, I_{ECT} is not fully suppressed when $v > u$. This could be due to other ABSs at higher V_{PG} that contribute to I_{ECT} or higher V_{PG} increasing tunneling rates via gate cross-coupling. Similar observations of the V_{PG} dependence reported here are reproduced in two more devices (Fig. S4 [29]).

Application of a Zeeman field lifts the Kramers' degeneracy of the ABS and the QDs. The spin splitting of the QDs makes their charge transitions spin polarized: The addition energy from N to $N+1$ electrons becomes lower (spin down, $\downarrow$), and that from $N+1$ to $N+2$ becomes higher (spin up, $\uparrow$) [35]. We, thus, control the spins of the electrons participating in CAR and ECT by selecting the corresponding charge transitions [15]. The odd states of the ABS split in energy, leading to two possible excitations from the ground state $|S\rangle$: either to $|D\downarrow\rangle$ with an energy $E_\downarrow = E_{\mathrm{ABS}} - E_Z/2$ or to $|D\uparrow\rangle$ with an energy $E_\uparrow = E_{\mathrm{ABS}} + E_Z/2$, where E_Z is the Zeeman splitting of the ABS [25].

Figure 3(a) shows schematically the process of ECT in the presence of a Zeeman field when both QDs are tuned to the $\uparrow$ transition. Again, this process can take place via two paths. In the first path (marked in gray), an $\uparrow$ electron from one lead populates the $|D\uparrow\rangle$ state of the ABS. Then, the ABS is emptied by emitting an $\uparrow$ electron to the other lead through the QD. In the second process (marked by the dashed green arrow), a hole from one lead hops into the ABS, exciting it into the $|D\downarrow\rangle$ state. The ABS then relaxes by emitting a hole to the other lead. The energies of the intermediate states in the two paths, $|D\uparrow\rangle$ and $|D\downarrow\rangle$, are split and the interference pattern is, thus, modified. The ECT-induced current is now of the form

$$I_{\mathrm{ECT}}^{\uparrow\uparrow} \propto \left| \frac{u^2}{E_\uparrow} - \frac{v^2}{E_\downarrow} \right|^2. \tag{3}$$

Since $E_\downarrow < E_\uparrow$, ECT is stronger when the ABS is holelike (large v) as seen in the $\uparrow\uparrow$ panel in Fig. 3(c). Analogously, the ECT is higher when the ABS is electronlike ($u > v$) and both QDs are tuned to the $\downarrow$ transition.

CAR-induced currents are also modified by the Zeeman splitting of the ABS doublet state. CAR takes place in two paths involving both levels [shown schematically in Fig. 3(b)]. In one path (marked by the dashed green arrow), the ABS occupies the $|D\downarrow\rangle$ state by receiving a $\downarrow$ electron from one lead and is emptied by receiving an $\uparrow$ electron from the other lead. In the second path (marked in gray), the order is reversed and the ABS passes through the $|D\uparrow\rangle$ state. The probability for the CAR process is now

$$I_{\mathrm{CAR}}^{\uparrow\downarrow} \propto \left| \frac{uv}{E_\downarrow} + \frac{uv}{E_\uparrow} \right|^2. \tag{4}$$

This probability peaks at the ABS energy minimum, as seen in the relevant panel in Fig. 3(c). Note that the expected CAR peak remains symmetric in μ, in contrast to ECT. Figure 3(d) shows the measured I_{CAR} and I_{ECT} under the application of $\vec{B} = 80$ mT along the nanowire direction, sufficient to fully spin polarize the QDs ($E_{\mathrm{Zeeman}}^{\mathrm{QD}} \approx 200$ μeV) and split the energy of the ABS ($E_Z \approx 100$ μeV; see Refs. [15,36]). Spin-orbit coupling in the nanowire allows for spin-flipping processes—equal-spin CAR and opposite-spin ECT—to take place [15], allowing us to measure ECT and CAR in all possible spin configurations. I_{CAR} is symmetric around the ABS energy minimum and is generally larger for opposite-spin than equal-spin configurations. I_{ECT} in the $\uparrow\uparrow$ spin configuration is large when the ABS is holelike ($v > u$) and is suppressed when it is electronlike (large u). The destructive interference dip is shifted from the ABS

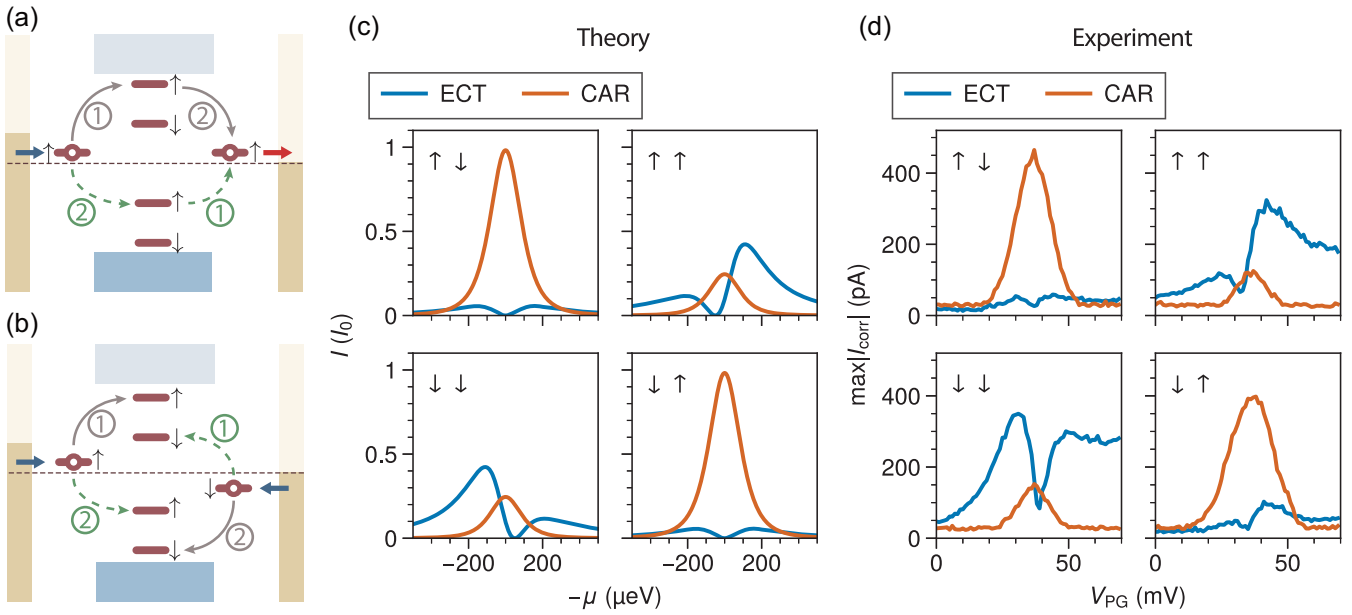

FIG. 3. CAR and ECT mediated by spin-polarized ABS. (a) ECT process mediated by a spin-polarized ABS between QDs in the ↑↑ spin configuration. (b) CAR process mediated by spin-polarized ABS between QDs in the ↑↓ spin configuration. (c) Calculation of the transmission probability of ECT and CAR via an atomic-limit ABS as a function μ at the four possible spin configurations of the QDs. Spin-orbit coupling is included in the calculation as a small spin-flipping factor ($\sigma = 0.2$) to allow for opposite-spin ECT and same-spin CAR (see Supplemental Material [29] for model details). Other model parameters are $\Gamma = 160$ μeV and $E_Z = 100$ μeV. (d) A high-resolution CAR and ECT amplitudes while tuning V_{PG} with $\vec{B} = 80$ mT (applied along the nanowire direction) at the four possible spin configurations of the QDs.

minimum toward lower V_{PG}. The opposite trend is observed in the ↓↓ spin configuration: I_{ECT} is slightly larger when the ABS is electronlike, and the interference dip is shifted toward higher values of V_{PG}. I_{ECT} in the opposite-spin configuration is nearly symmetric around the ABS minimum and is generally suppressed with respect to I_{ECT} in the equal-spin configuration. Thus, all of the qualitative predictions of the model [24] are verified in the measurements.

So far, we discuss the dependence of CAR and ECT magnitudes as a function of the ABS charge at zero and finite Zeeman field. In the following, we report on the dependence of CAR and ECT on the direction of the applied magnetic field $\vec{B}$, at fixed V_{PG}. We measure a second device, B, with a longer superconducting segment (approximately 350 nm, much larger than the superconducting coherence length in the Al film) and no Pt layer on top of the Al. The schematic in Fig. 4(h) indicates the angles θ and φ defining the field direction of $\vec{B}$. The QDs are set to the ↓↑ spin configuration, and V_{PG} is selected such that ECT is stronger than CAR when the field is parallel to the nanowire (see Fig. S6 [29] for the other spin configurations). Figures 4(a) and 4(b) show I_{CAR} and I_{ECT} when the angle of $\vec{B}$ is varied over a sphere. Figure 4(c) shows the energy of the lowest ABS at a similar V_{PG} (see Supplemental Material and Fig. S7 [29] for analysis details). All three quantities are anisotropic, and CAR and ECT amplitudes are overall negatively correlated to $E_\downarrow$ across the plotted globes, as expected for virtual tunneling processes. Below, we examine the rotational dependence of CAR and ECT along two exemplary meridians of the globe [dashed and dotted lines in Figs. 4(a)–4(c)] in order to separate anisotropy due to ABS energy from that caused by spin.

As discussed above, CAR and ECT amplitudes are inversely proportional to the ABS energy. This effect is highly visible in Fig. 4(e), where we plot $E_\downarrow$, I_{CAR}, and I_{ECT} along the meridian with $\varphi = -50°$ [dashed line in Figs. 4(a)–4(c)]. Here, $E_\downarrow$ is significantly modulated between approximately 170 μeV and approximately 50 μeV, and, accordingly, both I_{CAR} and I_{ECT} increase drastically at the energy minimum. In contrast, a very different pattern can be obtained when we rotate the magnetic field along the meridian of $\varphi = 40°$ [dotted line in Figs. 4(a)–4(c)]. Figure 4(f) shows that, along this meridian, $E_\downarrow$ changes by a small amount. As before, I_{CAR} is enhanced where $E_\downarrow$ is minimal. However, I_{ECT} varies in the opposite way and becomes completely suppressed around $\theta = 0$ (perpendicular to the nanowire axis). This suppression is generic across various V_{PG} values and, therefore, not explained by either the energy or the charge of the ABS. We attribute the reduction of opposite-spin ECT along this specific direction to spin blockade [15]. When the QDs select opposite spins, spin precession due to

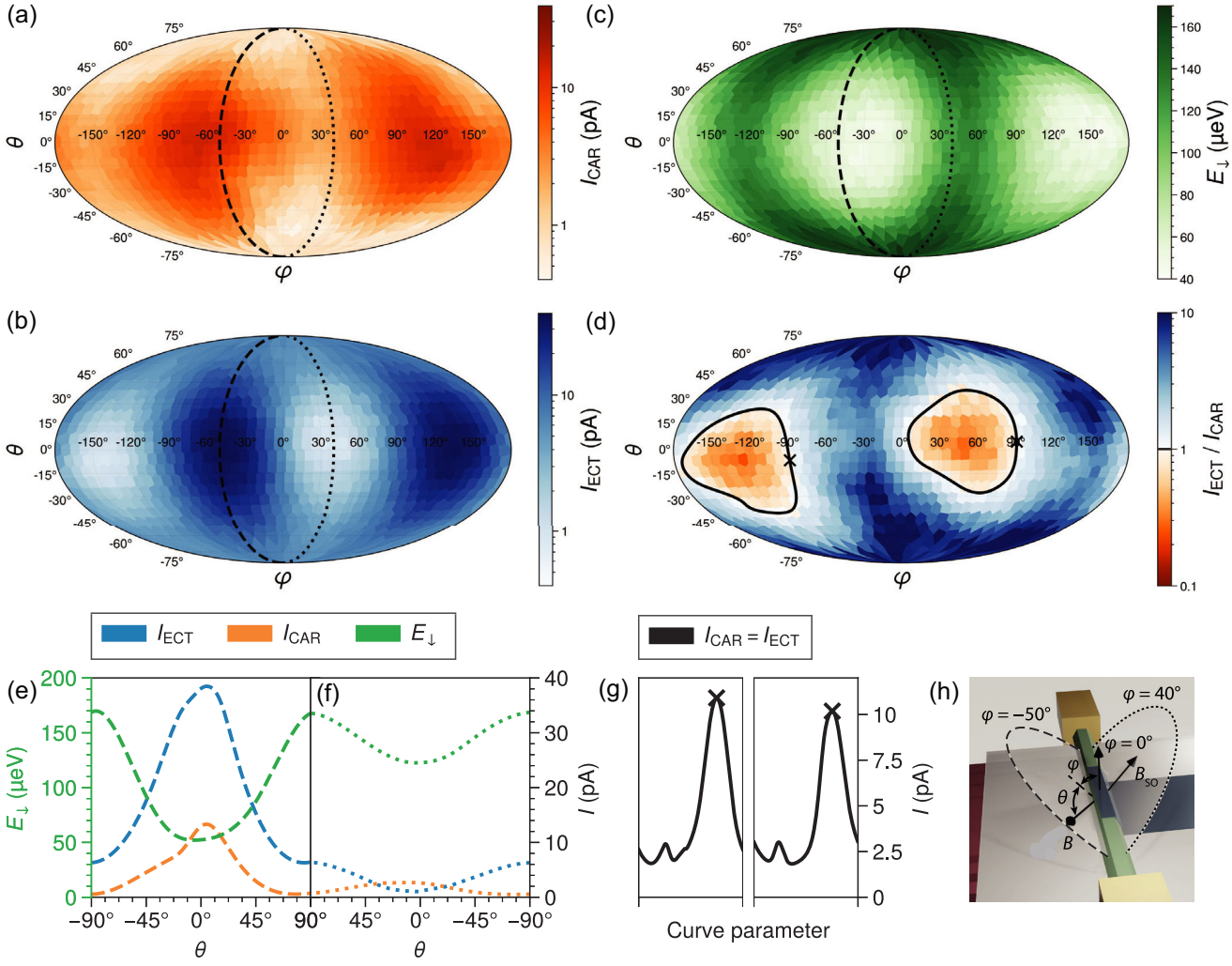

FIG. 4. Tuning CAR and ECT with magnetic field orientation. (a)–(d) Spherical plots: The center of every colored tile corresponds to a specific magnetic field orientation. Each panel is taken at fixed V_{PG} and $|\vec{B}| = 80$ mT. $V_{PG} = 475$ mV in (c), while $V_{PG} = 480$ mV in (a), (b), and (d). The QD spin configuration is $\downarrow\uparrow$ for all panels. See Fig. S7 [29] for data corresponding to other spin configurations. (a) CAR-induced current as a function of the magnetic field direction, extracted with the same method detailed in Fig. S1 [29] and used in the rest of the paper. (b) ECT-induced current as a function of the magnetic field orientation. (c) Energy of the lowest-energy ABS extracted from local tunneling spectroscopy as a function of the magnetic field orientation. (d) Ratio of the ECT and CAR currents from (b) and (a). Continuous lines highlight the locus of points where $I_{CAR} = I_{ECT}$; among them, the points with maximum current are marked with crosses. (e) Interpolation of data shown in (a)–(c) along the $\varphi = -50°$ meridian. (f) Interpolation of data shown in (a)–(c) along the $\varphi = +40°$ meridian. (g) I_{CAR} along the $I_{CAR} = I_{ECT}$ curves shown in (d). Negative-φ points are parametrized and plotted on the left, positive-φ points on the right. (h) Schematic defining θ and φ: $\theta = \pm 90°$ is the direction parallel to the nanowire. $\theta = \varphi = 0°$ is the direction perpendicular to the substrate.

spin-orbit coupling enables the presence of some I_{ECT} [24]. However, if the applied $\vec{B}$ is parallel to the effective spin-orbit field $\vec{B}_{SO}$, no spin precession occurs, and, therefore, ECT is suppressed between QDs with opposite spins [37,38]. The observation of this type of spin blockade reveals the orientation of the spin-orbit field. Compared to prior works measuring the spin-orbit field direction in hybrid nanowires via superconducting gap size anisotropy, the method presented here using spin conservation to detect the $\vec{B}_{SO}$ direction is less prone to other effects such as orbital depairing and g-factor anisotropy (Fig. S8 [29]).

With these two effects in mind, we summarize the angle dependence of CAR and ECT over the entire sphere as follows. First, there exists one special $\vec{B}$ direction along which equal-spin CAR and opposite-spin ECT are strongly suppressed (see Fig. S7 [29] for other spin combinations). We interpret this as a spin-blockade effect and its direction as that of the spin-orbit field. Away from this blockaded

direction, multiple factors compete to influence the amplitudes of CAR and ECT, such as the angle between $\vec{B}$ and $\vec{B}_{\mathrm{SO}}$ and the energy of the mediating ABS.

This combination of anisotropic ABS energy and spin-orbit coupling makes the $\vec{B}$ direction dependence of CAR and ECT very rich, enabling further tuning of their relative amplitudes. Figure 4(d) shows the ratio between I_{ECT} and I_{CAR} as a function of the $\vec{B}$ orientation. Here, due to the aforementioned influence of the ABS charge, I_{ECT} is larger than I_{CAR} on most of the sphere. However, since ECT is suppressed along a specific direction, the ratio between I_{ECT} and I_{CAR} can be inverted. Such tunability allows for $I_{\mathrm{CAR}} = I_{\mathrm{ECT}}$, the sweet spot essential for the realization of poor man's Majoranas in a minimal Kitaev chain [3,8]. Figure 4(d) shows with continuous lines the locus of points where $(I_{\mathrm{ECT}}/I_{\mathrm{CAR}}) = 1$, and Fig. 4(f) reports the corresponding current values, highlighting with crosses the points where $I_{\mathrm{CAR}}(= I_{\mathrm{ECT}})$ is maximal. It is, therefore, evident that the $\vec{B}$ dependence of CAR and ECT not only enables the tuning to the $I_{\mathrm{CAR}} = I_{\mathrm{ECT}}$ sweet spot, but also allows optimization of their strengths.

In summary, we have measured ECT- and CAR-induced currents mediated by ABSs formed in a proximitized InSb nanowire. We show that the amplitudes of both processes depend on the charge of the ABSs and are, thus, highly tunable via electrostatic gating. Particularly, we show that ECT is significantly suppressed when the ABS is charge neutral due to destructive interference originating from fermionic exchange statistics. Furthermore, we examine how the interference pattern and the balance between ECT and CAR is shifted when the applied magnetic field spin polarizes the QDs and splits the energy of the ABS. Finally, we measure how the magnetic field orientation modifies both the energy of the ABS and the effect of spin-orbit coupling, adding another independent knob to tune CAR and ECT. These results demonstrate deterministic control of the relative amplitudes of CAR and ECT, forming the foundation of realizing an artificial Kitaev chain [8].

Raw data presented in this work, the data processing and plotting code, and the code used for the theory calculations are available [39].

This work has been supported by the Dutch Organization for Scientific Research (NWO) and Microsoft Corporation Station Q. We thank Gijs de Lange for helpful discussions.

G. W., G. P. M., N. v. L., A. B., F. Z., and D. v. D. fabricated the devices. G. W., T. D., S. L. D. t. H., A. B., and D. X. performed the electrical measurements. T. D. and G. W. designed the experiment. A. B., G. W., and T. D. analyzed the data. A. B., T. D., and L. P. K. prepared the manuscript with input from all authors. T. D. and L. P. K. supervised the project. C.-X. L. developed the theoretical model with input from M. W. S. G., G. B., and E. P. A. M. B. performed InSb nanowire growth.

[1] A. Y. Kitaev, *Unpaired Majorana Fermions in Quantum Wires*, Phys. Usp. **44**, 131 (2001).

[2] J. D. Sau and S. D. Sarma, *Realizing a Robust Practical Majorana Chain in a Quantum-Dot-Superconductor Linear Array*, Nat. Commun. **3**, 964 (2012).

[3] M. Leijnse and K. Flensberg, *Parity Qubits and Poor Man's Majorana Bound States in Double Quantum Dots*, Phys. Rev. B **86**, 134528 (2012).

[4] I. C. Fulga, A. Haim, A. R. Akhmerov, and Y. Oreg, *Adaptive Tuning of Majorana Fermions in a Quantum Dot Chain*, New J. Phys. **15**, 045020 (2013).

[5] P. Recher, E. V. Sukhorukov, and D. Loss, *Andreev Tunneling, Coulomb Blockade, and Resonant Transport of Nonlocal Spin-Entangled Electrons*, Phys. Rev. B **63**, 165314 (2001).

[6] D. Beckmann, H. B. Weber, and H. v. Löhneysen, *Evidence for Crossed Andreev Reflection in Superconductor-Ferromagnet Hybrid Structures*, Phys. Rev. Lett. **93**, 197003 (2004).

[7] S. Russo, M. Kroug, T. M. Klapwijk, and A. F. Morpurgo, *Experimental Observation of Bias-Dependent Nonlocal Andreev Reflection*, Phys. Rev. Lett. **95**, 027002 (2005).

[8] T. Dvir, G. Wang, N. v. Loo, C.-X. Liu, G. P. Mazur, A. Bordin, S. L. D. t. Haaf, J.-Y. Wang, D. v. Driel, F. Zatelli, X. Li, F. K. Malinowski, S. Gazibegovic, G. Badawy, E. P. A. M. Bakkers, M. Wimmer, and L. P. Kouwenhoven, *Realization of a Minimal Kitaev Chain in Coupled Quantum Dots*, Nature (London) **614**, 445 (2023).

[9] M.-S. Choi, C. Bruder, and D. Loss, *Spin-Dependent Josephson Current through Double Quantum Dots and Measurement of Entangled Electron States*, Phys. Rev. B **62**, 13569 (2000).

[10] M. Leijnse and K. Flensberg, *Coupling Spin Qubits via Superconductors*, Phys. Rev. Lett. **111**, 060501 (2013).

[11] F. Hassler, G. Catelani, and H. Bluhm, *Exchange Interaction of Two Spin Qubits Mediated by a Superconductor*, Phys. Rev. B **92**, 235401 (2015).

[12] L. Gonzalez Rosado, F. Hassler, and G. Catelani, *Long-Range Exchange Interaction between Spin Qubits Mediated by a Superconducting Link at Finite Magnetic Field*, Phys. Rev. B **103**, 035430 (2021).

[13] M. Spethmann, X.-P. Zhang, J. Klinovaja, and D. Loss, *Coupled Superconducting Spin Qubits with Spin-Orbit Interaction*, Phys. Rev. B **106**, 115411 (2022).

[14] M. Spethmann, S. Bosco, A. Hofmann, J. Klinovaja, and D. Loss, *High-Fidelity Two-Qubit Gates of Hybrid Superconducting-Semiconducting Singlet-Triplet Qubits*, arXiv:2304.05086.

[15] G. Wang, T. Dvir, G. P. Mazur, C.-X. Liu, N. v. Loo, S. L. D. t. Haaf, A. Bordin, S. Gazibegovic, G. Badawy, E. P. A. M. Bakkers, M. Wimmer, and L. P. Kouwenhoven, *Singlet and Triplet Cooper Pair Splitting in Hybrid Superconducting Nanowires*, Nature (London) **612**, 448 (2022).

[16] L. Hofstetter, S. Csonka, J. Nygård, and C. Schönenberger, *Cooper Pair Splitter Realized in a Two-Quantum-Dot y-Junction*, Nature (London) **461**, 960 (2009).
[17] L. Hofstetter, S. Csonka, A. Baumgartner, G. Fülöp, S. d'Hollosy, J. Nygård, and C. Schönenberger, *Finite-Bias Cooper Pair Splitting*, Phys. Rev. Lett. **107**, 136801 (2011).
[18] A. Das, Y. Ronen, M. Heiblum, D. Mahalu, A. V. Kretinin, and H. Shtrikman, *High-Efficiency Cooper Pair Splitting Demonstrated by Two-Particle Conductance Resonance and Positive Noise Cross-Correlation*, Nat. Commun. **3**, 1165 (2012).
[19] J. Schindele, A. Baumgartner, and C. Schönenberger, *Near-Unity Cooper Pair Splitting Efficiency*, Phys. Rev. Lett. **109**, 157002 (2012).
[20] J. Schindele, A. Baumgartner, R. Maurand, M. Weiss, and C. Schönenberger, *Nonlocal Spectroscopy of Andreev Bound States*, Phys. Rev. B **89**, 045422 (2014).
[21] J. Danon, A. B. Hellenes, E. B. Hansen, L. Casparis, A. P. Higginbotham, and K. Flensberg, *Nonlocal Conductance Spectroscopy of Andreev Bound States: Symmetry Relations and BCS Charges*, Phys. Rev. Lett. **124**, 036801 (2020).
[22] G. C. Ménard, G. L. R. Anselmetti, E. A. Martinez, D. Puglia, F. K. Malinowski, J. S. Lee, S. Choi, M. Pendharkar, C. J. Palmstrøm, K. Flensberg, C. M. Marcus, L. Casparis, and A. P. Higginbotham, *Conductance-Matrix Symmetries of a Three-Terminal Hybrid Device*, Phys. Rev. Lett. **124**, 036802 (2020).
[23] G. Fülöp, F. Domínguez, S. d'Hollosy, A. Baumgartner, P. Makk, M. H. Madsen, V. A. Guzenko, J. Nygård, C. Schönenberger, A. Levy Yeyati, and S. Csonka, *Magnetic Field Tuning and Quantum Interference in a Cooper Pair Splitter*, Phys. Rev. Lett. **115**, 227003 (2015).
[24] C.-X. Liu, G. Wang, T. Dvir, and M. Wimmer, *Tunable Superconducting Coupling of Quantum Dots via Andreev Bound States in Semiconductor-Superconductor Nanowires*, Phys. Rev. Lett. **129**, 267701 (2022).
[25] E. J. H. Lee, X. Jiang, M. Houzet, R. Aguado, C. M. Lieber, and S. D. Franceschi, *Spin-Resolved Andreev Levels and Parity Crossings in Hybrid Superconductor–Semiconductor Nanostructures*, Nat. Nanotechnol. **9**, 79 (2014).
[26] Q. Wang, S. L. ten Haaf, I. Kulesh, D. Xiao, C. Thomas, M. J. Manfra, and S. Goswami, *Triplet Cooper Pair Splitting in a Two-Dimensional Electron Gas*, arXiv:2211.05763.
[27] S. Heedt, M. Quintero-Pérez, F. Borsoi, A. Fursina, N. van Loo, G. P. Mazur, M. P. Nowak, M. Ammerlaan, K. Li, S. Korneychuk *et al.*, *Shadow-Wall Lithography of Ballistic Superconductor–Semiconductor Quantum Devices*, Nat. Commun. **12**, 1 (2021).
[28] F. Borsoi, G. P. Mazur, N. van Loo, M. P. Nowak, L. Bourdet, K. Li, S. Korneychuk, A. Fursina, J.-Y. Wang, V. Levajac, E. Memisevic, G. Badawy, S. Gazibegovic, K. van Hoogdalem, E. P. A. M. Bakkers, L. P. Kouwenhoven, S. Heedt, and M. Quintero-Pérez, *Single-Shot Fabrication of Semiconducting–Superconducting Nanowire Devices*, Adv. Funct. Mater. **31**, 2102388 (2021).
[29] See Supplemental Material at http://link.aps.org/supplemental/10.1103/PhysRevX.13.031031 for a complete theoretical model and additional supporting data.
[30] T. O. Rosdahl, A. Vuik, M. Kjaergaard, and A. R. Akhmerov, *Andreev Rectifier: A Nonlocal Conductance Signature of Topological Phase Transitions*, Phys. Rev. B **97**, 045421 (2018).
[31] F. Domínguez and A. L. Yeyati, *Quantum Interference in a Cooper Pair Splitter: The Three Sites Model*, Physica (Amsterdam) **75E**, 322 (2016).
[32] A. Tsintzis, R. S. Souto, and M. Leijnse, *Creating and Detecting Poor Man's Majorana Bound States in Interacting Quantum Dots*, Phys. Rev. B **106**, L201404 (2022).
[33] J. Bauer, A. Oguri, and A. C. Hewson, *Spectral Properties of Locally Correlated Electrons in a Bardeen–Cooper–Schrieffer Superconductor*, J. Phys. Condens. Matter **19**, 486211 (2007).
[34] A. Pöschl, A. Danilenko, D. Sabonis, K. Kristjuhan, T. Lindemann, C. Thomas, M. J. Manfra, and C. M. Marcus, *Nonlocal Conductance Spectroscopy of Andreev Bound States in Gate-Defined InAs/Al Nanowires*, Phys. Rev. B **106**, L241301 (2022).
[35] R. Hanson, L. P. Kouwenhoven, J. R. Petta, S. Tarucha, and L. M. K. Vandersypen, *Spins in Few-Electron Quantum Dots*, Rev. Mod. Phys. **79**, 1217 (2007).
[36] G. P. Mazur, N. v. Loo, J. Y. Wang, T. Dvir, G. Wang, A. Khindanov, S. Korneychuk, F. Borsoi, R. C. Dekker, G. Badawy, P. Vinke, S. Gazibegovic, E. P. A. M. Bakkers, M. Quintero-Perez, S. Heedt, and L. P. Kouwenhoven, *Spin-Mixing Enhanced Proximity Effect in Aluminum-Based Superconductor-Semiconductor Hybrids*, arXiv:2202.10230.
[37] A. Hofmann, V. F. Maisi, T. Krähenmann, C. Reichl, W. Wegscheider, K. Ensslin, and T. Ihn, *Anisotropy and Suppression of Spin-Orbit Interaction in a GaAs Double Quantum Dot*, Phys. Rev. Lett. **119**, 176807 (2017).
[38] J.-Y. Wang, G.-Y. Huang, S. Huang, J. Xue, D. Pan, J. Zhao, and H. Xu, *Anisotropic Pauli Spin-Blockade Effect and Spin–Orbit Interaction Field in an InAs Nanowire Double Quantum Dot*, Nano Lett. **18**, 4741 (2018).
[39] A. Bordin, G. Wang, and T. Dvir, *Controlled Crossed Andreev Reflection and Elastic Co-Tunneling Mediated by Andreev Bound States (1.0)*, Zenodo, (2022), 10.5281/zenodo.7395016.